Optical metasurfaces for polarization-controlled beam shaping

Ori Avayu,* Omri Eisenbach, Ran Ditcovski, and Tal Ellenbogen

Department of Physical Electronics, Fleischman Faculty of Engineering, Tel Aviv University, Tel Aviv 69978, Israel
**Corresponding author: oria@post.tau.ac.il*

Received March 20, 2014; revised May 5, 2014; accepted May 20, 2014;
posted May 22, 2014 (Doc. ID 207725); published June 24, 2014

We have developed multifunctional optical beam shapers based on plasmonic metasurfaces. The metasurfaces are composed of subwavelength-spaced polarization- and wavelength-selective optical nanoantennas that allow encoding several beam shapers on a single element. We demonstrate numerically and experimentally beam shapers that can be used to switch between arbitrary beam shapes. We specifically demonstrate switching between one-dimensional Airy and Gaussian beams, Hermite–Gaussian beams of different orders, and two-dimensional Airy and Bessel beams. These beam shapers can be used as integrated optical elements in applications that require more than one laser beam shape. © 2014 Optical Society of America

OCIS codes: (230.0230) Optical devices; (240.0240) Optics at surfaces; (090.0090) Holography; (050.0050) Diffraction and gratings; (160.3918) Metamaterials.
http://dx.doi.org/10.1364/OL.39.003892

Recent progress in nanofabrication tools, with advances in the understanding of the interaction between light and nanostructures, has opened a new frontier in optical sciences—the development of the commonly named optical metamaterials and metasurfaces [1,2]. Much of the attention that this field receives is due to the fact that it enables engineering materials with unnatural optical properties that cannot be mimicked by conventional optical materials. This can potentially enhance the toolbox of components for optical manipulations. Optical metamaterials are usually constructed by lattices of nanoscale dielectric or metallo-dielectric building blocks, spaced at subwavelength distances. The optical response of metamaterials is governed by the properties and arrangement of their subwavelength building blocks in analogy to the arrangement of atoms and molecules in natural materials.

In recent years, many groups have demonstrated optical metamaterials and metasurfaces with new and exciting physical properties, including negative index of refraction [3], which was used to demonstrate cloaking [4]; hyperbolic dispersion, which was used to show enhanced spontaneous emission; a low effective index of refraction; and superlensing [5–8], engineered refraction from ultrathin subwavelength layers [9], and chromatic polarizers, which were proposed for anticounterfeiting applications and polarimetry [10]. In addition, metasurfaces were used by several groups to develop novel beam-shaping elements [7,11–16].

The metasurface-based beam-shaping elements that have been demonstrated up to date were designed for a single beam shaping functionality. Here, we present the use of metasurfaces composed of arrays of rod- and cross-shaped optical metallic nanoantennas, as new means for designing passive optical beam shapers with multiple beam shaping functionalities. The nanoantennas have a resonance operating frequency that originates from the coupling of incident light to localized surface plasmons (LSPs) [17]. This coupling results in an increase of the absorption and scattering cross section of the nanoantenna, which can grow to several times its physical dimensions [18]. The effective resonance wavelength λ_{eff} can be described empirically by a linear law [19]:

$$\lambda_{\mathrm{eff}} = n_1 + n_2\left(\frac{\lambda}{\lambda_p}\right), \tag{1}$$

where λ is the free-space wavelength, λ_p is the plasma wavelength in the bulk metal, and n_1 and n_2 are coefficients that depend on the surrounding dielectric and the antenna geometry, respectively. The effect of antenna geometry and anisotropy on its resonance was also studied in detail before [20]. Another way to engineer a metasurface response is by controlling the interaction between individual nanoantennas through modifying their spacing and arrangements. For example, for rod nanoantennas placed in an end-to-end configuration, decreasing the distance between the nanoantennas results in a red shift of the LSP resonance, whereas for a side-by-side configuration, decreasing their distance will result in a blue shift [21].

In order to develop metasurfaces for multifunctional beam shaping, we combined the local polarization and wavelength selectivity of metasurfaces with methods from computer-generated holograms (CGHs) for phase and amplitude modulation.

In a conventional CGH, the phase and amplitude of an input beam are encoded onto a mask, according to a desired far-field output beam. Specifically, in the case of a binary CGH (bCGH), the two-dimensional (2D) phase and amplitude mask encoding in the transmission function of the mask, $t(x,y)$, is given by [22]

$$t(x,y) = \begin{cases} 1 & \cos\left(\frac{2\pi}{\Lambda}x - \phi(x,y)\right) - \cos(\pi q(x,y)) \geq 0 \\ 0 & \text{otherwise} \end{cases}, \tag{2}$$

where Λ is the carrier wavelength and $\phi(x,y)$ is the phase of the Fourier transform of the desired beam shape. The amplitude of the Fourier transform of the desired beam shape, $A(x,y)$, is introduced through the relation

$A(x,y) = \sin(\pi q(x,y))$. $A(x,y)$ is normalized to the range 0–1 and $\phi(x,y)$ is in the range 0–2π. The desired beam function is obtained at the first diffraction order in the far field by the Fourier transform of the encoding $U(x',y') \propto \mathcal{F}(A(x,y)\exp(i\phi(x,y)))$. We enhance this concept by constructing the CGH from metasurfaces that introduce strong local polarization and wavelength dependencies. These provide additional degrees of freedom to design the metasurface-based bCGH (mCGH). The transmission function of the mask in this case also becomes a function of the polarization and wavelength of the beam. Formally,

$$t(x,y,\lambda,\hat{e}) = t_x(x,y,\lambda)e_x + t_y(x,y,\lambda)e_y, \tag{3}$$

where λ and $\hat{e}$ are the wavelength and normalized polarization vector of light, respectively. The subscripts stand for x and y polarizations, and $t_{x,y}(x,y,\lambda)$ becomes a function of $\phi_{x,y}(x,y,\lambda)$ and $q_{x,y}(x,y,\lambda)$. For each polarization input, x and y, our mask, therefore, acts as a conventional bCGH, independent of the perpendicular polarization, and takes the form of Eq. (2). In this case, the transmitted power $T(x,y,\lambda,\varphi)$ becomes

$$T(x,y,\lambda,\varphi) = T_x(x,y,\lambda)\cos^2\varphi + T_y(x,y,\lambda)\sin^2\varphi, \tag{4}$$

where T_x and T_y are the transmitted power fields aligned along the x and y axes, respectively, and φ is the angle between the polarization vector and x axis. Perpendicularly polarized incident beams will, therefore, experience independent diffraction. In the same manner, the wavelength selectivity of the mCGH introduces an additional degree of freedom, which allows encoding of multiple beam shaping functionalities in a single metasurface.

As a proof of concept, we have designed beam-shaping metasurfaces with a dual response that is controlled by the state of polarization. To construct the metasurfaces, we use three types of nanoantenna building blocks—vertically oriented rods, which correspond to areas where $t_x(x,y) = 1$; horizontally oriented rods, which correspond to areas where $t_y(x,y) = 1$; and crosses, which correspond to areas where $t_x(x,y) = t_y(x,y) = 0$. In areas where $t_x(x,y) = t_y(x,y) = 1$, the surface was free of nanoantennas. For simplicity, the frequency response was chosen to be the same for both x and y polarizations.

To fabricate the samples, we used standard e-beam lithographic writing of the masks. Poly(methyl methacrylate) was spin-coated on top of indium tin oxide-coated glass, followed by evaporation of 40 nm of aluminum and a subsequent lift-off process. Aluminum was chosen for its CMOS compatibility, and high plasma frequency, which enables tuning its LSP resonance over the entire visible spectrum [23]. The selected rod nanoantenna dimensions were $l = 140$ nm, $w = 40$ nm, and $t = 40$ nm, where l, w, and t are, respectively, the length, width, and thickness of the rod nanoantennas. These parameters give a strong polarized scattering response in the red part of the visible spectrum (operation wavelength was $\lambda = 632$ nm). The crosses had the same thicknesses and widths, but the arm lengths were extended to 170 nm in order to correct the shift of their resonance with respect to that of the rod-shaped nanoantennas. It was shown previously [10] that for a single layer of cross nanoantennas with similar parameters, the simulated and measured extinction ratios (areas where $t(x,y) = 1$ to $t(x,y) = 0$) are greater than 15 and 2, respectively. The difference between measurements and simulations was attributed to fabrication imperfections. The period of the 2D lattices was subwavelength ($p = 220$ nm) in order to eliminate grating effects. On the other hand, the nanoantennas are still spaced at sufficiently large distances so that the effects of coupling between adjacent nanoantennas on the function of the metasurface are minimized [21].

As a first proof of concept, we chose to demonstrate switching between Gaussian beams and Airy beams that are nearly nondiffracting beams with unique properties [24,25]. Figure 1 demonstrates the fabricated mCGH and the experimental concept. We used a binary phase-only mCGH. The size of the mask was $100 \times 100\ \mu\mathrm{m}^2$ and the period of modulation in the x direction was $\Lambda = 5\ \mu\mathrm{m}$ for both polarizations. This way both beams diffract at the same angle ($\alpha = 8.4°$) and achieve a perfect overlap. The phase of the two beams was changed between zero phase, $\phi_x(x,y) = 0$, for generating a Gaussian diffraction and a cubic phase, $\phi_y(x,y) = y^3/a$, generating an Airy beam at the far field [24,25], where a is equal to $1.59\ \mathrm{e}^{-7}\ \mu\mathrm{m}^3$. Figure 1(a) shows an SEM image of the dual-functionality mCGH. The inset reveals the nanoscale structure of the element, which locally changes between horizontal rods, vertical rods, and crosses according to the mask function $t(x,y,\lambda,\hat{e})$. Figures 1(b) and 1(c) show polarized bright-field optical microscope images (the horizontal axis is stretched for viewing purposes). Some regions of the mask are dimmer than others due to imperfections in the fitting of the transmission of

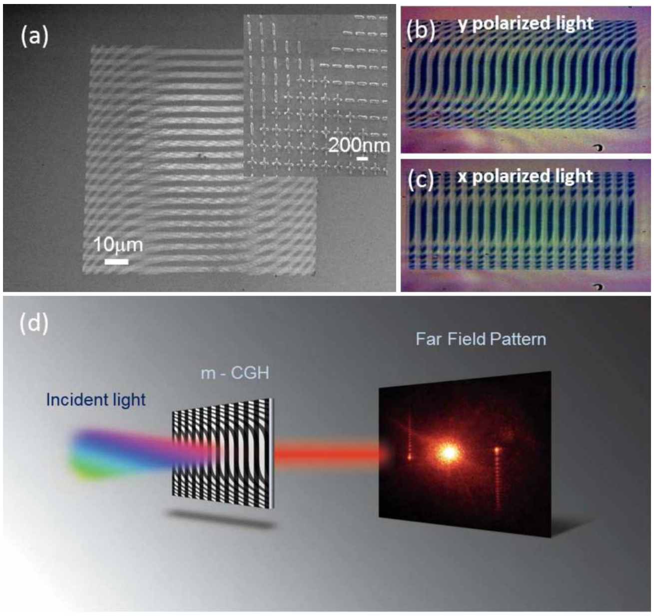

Fig. 1. (a) A scanning electron microscope (SEM) image of the Airy–Gaussian mCGH. The inset shows the mCGH rod and cross-shaped building blocks. (b) and (c) Polarized bright-field optical images of the mCGH. The images are stretched for viewing purposes. (d) Artistic view of the experiment. Polarized light is normally incident on the mCGH. The emerging beams at the far field are imaged on a screen in transmission and reflection.

the metasurface areas of the cross nanoantennas and those of the rod nanoantennas; however, the polarization response is still observed easily. Fitting of the transmission function can be done by either modifying the spacing between the nanoantennas or by using other fabrication approaches such as using multilayers.

The mask appears blue in transmission due to tuning of the metasurface to operate in the red part of the visible spectrum. Figure 1(d) shows an artistic view of the operation of the element. We used the output of a He–Ne laser, which was normally incident on the CGH mask and the beam polarization was controlled with a Glan–Thompson-type polarizer. The diffraction orders were then imaged on a screen or camera in transmission and reflection and captured for analysis.

Figures 2(a) and 2(b) show the simulated transmission from the mask at the two polarizations. The color bar indicates the normalized absolute value of the transmitted fields. The simulated far-field image [Figs. 2(c) and 2(d)] was obtained by performing a Fourier transform of the mask function $t(x, y, \lambda, \vec{e})$ for the two mask components. Figures 2(e) and 2(f) show the experimental results of the polarized diffraction from the fabricated sample. The center of the image was blocked artificially to eliminate zero-order transmission. The Gaussian [Fig. 2(e)] and Airy [Fig. 2(f)] patterns are obtained at the first diffraction order for the two perpendicular input polarizations. The beam shapes and the measured diffraction angle ($\alpha = 8.4°$) showed good agreement with the simulated results.

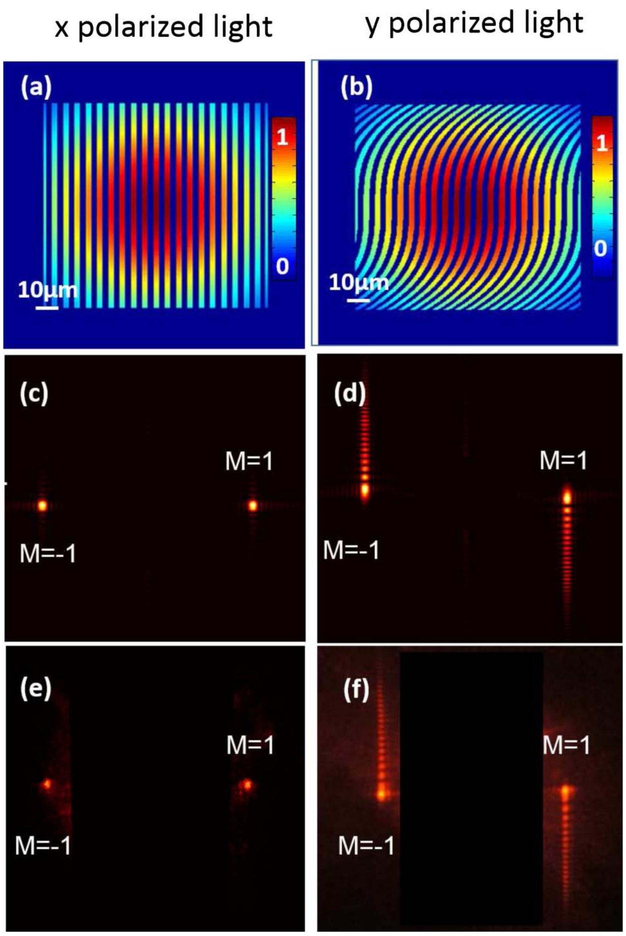

Fig. 2. Simulations and experimental results of the Airy–Gaussian mCGH mask. Simulated normalized transmission patterns through the mCGH with (a) zero phase, $\phi_x(x, y) = 0$, and (b) a cubic phase, $\phi_y(x, y) = y^3/a$. (c) and (d) show the simulated far-field beams. (e) and (f) show the experimental switching between (e) the Gaussian beam and (f) the Airy beam at the first diffraction orders.

To show the diversity of the method, we fabricated and tested additional mCGHs generating Hermite–Gaussian (HG) beams. These beams match the spherical symmetry of the resonators [26] and can be used in applications where phase dislocations are important [27]. Figures 3(a) and 3(b) show a schematic view of the mCGH that was designed to switch between the lowest-order HG beam and the first-order HG beam. The phases of the HG mask for x and y are given by $\phi_x(x, y) = \pi/2 \cdot \mathrm{sign}(y)$ and $\phi_y(x, y) = 0$, respectively. Figures 3(c) and 3(d) show the first diffraction order of the two modes, clearly demonstrating the switching between the desired modes.

Thus far, we have shown one-dimensional beam shaping, although the flexibility of the mCGH readily allows us to also generate 2D beam shapes, which are important for a variety of applications [27–29]. We, therefore, also demonstrated an mCGH that can switch between Bessel beams and 2D Airy beams. The horizontal mCGH phase term is then given by $\phi_x(x, y) = x^3/a + y^3/a$, corresponding to a 2D Airy beam, and the vertical mCGH phase and amplitude terms are $\phi_y(x, y) = 0$ and $q_y(x, y) = \sin^{-1}\{\sqrt{x^2 + y^2}\}$, respectively, $40\ \mu\mathrm{m} \leq x$, $y \leq 60\ \mu\mathrm{m}$, corresponding to the Fourier transform of a Bessel beam. The simulated and experimentally obtained beams, generated at the first diffraction order, at the two polarizations are presented in Fig. 4. The experimental results [Figs. 4(b) and 4(d)] agree well with the simulations [Figs. 4(a) and 4(c)].

In this work, we have demonstrated the development of an mCGH beam-shaping element that allows encoding multiple beam shapes on the same element and switching between different beam shapes by polarization or wavelength. Metasurfaces for single-purpose beam shaping

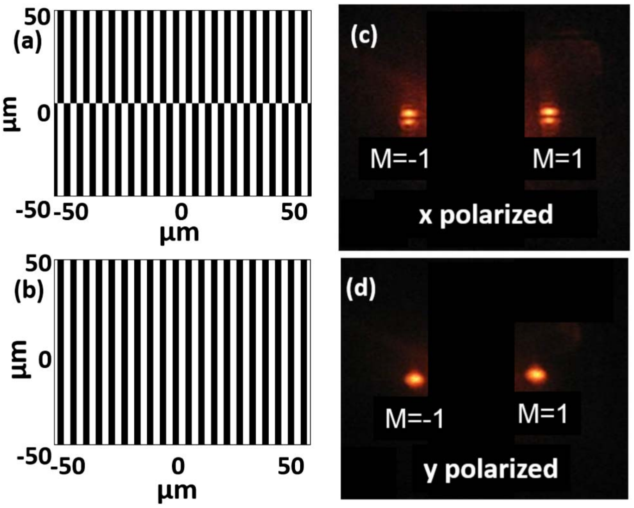

Fig. 3. Experimental results of the HG mCGH beam-shaping element. (a) and (b) show a schematic view of the mCGH mask pattern. (c) and (d) show the experimental result for switching between HG_{01} and HG_{00} beams.

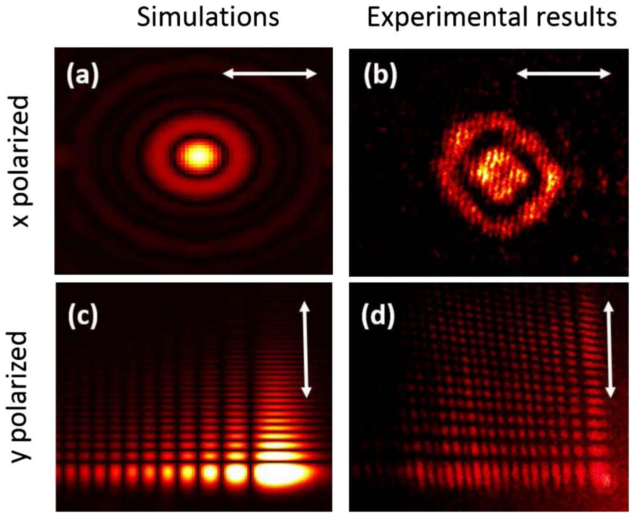

Fig. 4. Polarized diffraction from the mCGH designed to switch between 2D Airy and Bessel beams. (a) Simulated and (b) experimentally obtained Bessel beams at the first diffracted order. (c) Simulated and (d) experimentally obtained 2D Airy beams. The arrows indicate the input laser polarization.

were demonstrated in the past by several techniques, e.g., space-variant subwavelength gratings [7,11,12], nanoapertures [30], and V-groove nanoantennas [9,13,14]. Here, we have extended the toolbox for beam shaping by metasurfaces and have demonstrated multiple beam shaping functions in a single element working in both transmission and reflection. We show that the emerging beams can be independent and can be chosen per application. The multifunctional capabilities of the mCGHs, together with the ease of their design, low cost, and readily available fabrication tools, opens the door for a variety of interesting applications, including integrated beam shapers for stimulated emission depletion (STED) setups [27], polarization microscopy, and in-cavity multifunctional laser beam shapers.

This work was supported mainly by the Israeli Ministry of Trade and Labor—Kamin Program, Grant No. 51387, and was also supported partially by the Israeli Science Foundation, Grant No. 1331/13, and the European Commission Marie Curie Career Integration Grant No. 333821.

References

1. A. V. Kildishev, A. Boltasseva, and V. M. Shalaev, Science **339**, 1232009 (2013).
2. H. Chen, C. T. Chan, and P. Sheng, Nat. Mater. **9**, 387 (2010).
3. S. Tretyakov, I. Nefedov, A. Sihvola, S. Maslovski, and C. Simovski, J. Electromagn. Waves Appl. **17**, 695 (2003).
4. W. Cai, U. K. Chettiar, A. V. Kildishev, and V. M. Shalaev, Nat. Photonics **1**, 224 (2007).
5. J. Pendry, Phys. Rev. Lett. **85**, 3966 (2000).
6. J. Elser, R. Wangberg, V. A. Podolskiy, and E. E. Narimanov, Appl. Phys. Lett. **89**, 261102 (2006).
7. N. Fang, H. Lee, C. Sun, and X. Zhang, Science **308**, 534 (2005).
8. S. Enoch, G. Tayeb, P. Sabouroux, N. Guérin, and P. Vincent, Phys. Rev. Lett. **89**, 213902 (2002).
9. F. Aieta, P. Genevet, M. A. Kats, N. Yu, R. Blanchard, Z. Gaburro, and F. Capasso, Nano Lett. **12**, 4932 (2012).
10. T. Ellenbogen, K. Seo, and K. B. Crozier, Nano Lett. **12**, 1026 (2012).
11. L. Pang, M. Nezhad, U. Levy, C.-H. Tsai, and Y. Fainman, Appl. Opt. **44**, 2377 (2005).
12. U. Levy, C.-H. Tsai, L. Pang, and Y. Fainman, Opt. Lett. **29**, 1718 (2004).
13. F. Zhou, Y. Liu, and W. Cai, Opt. Express **21**, 4348 (2013).
14. N. Yu, P. Genevet, M. A. Kats, F. Aieta, J.-P. Tetienne, F. Capasso, and Z. Gaburro, Science **334**, 333 (2011).
15. C. Pfeiffer and A. Grbic, Phys. Rev. Lett. **110**, 197401 (2013).
16. F. Monticone, N. M. Estakhri, and A. Alù, Phys. Rev. Lett. **110**, 203903 (2013).
17. S. A. Maier, *Plasmonics: Fundamentals and Applications* (Springer, 2007).
18. D. D. Evanoff and G. Chumanov, J. Phys. Chem. B **108**, 13957 (2004).
19. L. Novotny, Phys. Rev. Lett. **98**, 266802 (2007).
20. C. J. Murphy, T. K. Sau, A. M. Gole, C. J. Orendorff, J. Gao, L. Gou, S. E. Hunyadi, and T. Li, J. Phys. Chem. B **109**, 13857 (2005).
21. P. K. Jain, S. Eustis, and M. A. El-Sayed, J. Phys. Chem. B **110**, 18243 (2006).
22. W. H. Lee, Appl. Opt. **18**, 3661 (1979).
23. P. West, S. Ishii, G. Naik, N. Emani, V. Shalaev, and A. Boltasseva, Laser Photon. Rev. **4**, 795 (2010).
24. G. A. Siviloglou, J. Broky, A. Dogariu, and D. N. Christodoulides, Opt. Lett. **33**, 207 (2008).
25. T. Ellenbogen and N. Voloch-Bloch, Nat. Photonics **3**, 395 (2009).
26. B. E. A. Saleh and M. C. Teich, *Fundamentals of Photonics*, 2nd ed. (Wiley-Interscience, 2007).
27. S. W. Hell and J. Wichmann, Opt. Lett. **19**, 780 (1994).
28. P. Polynkin, M. Kolesik, J. V. Moloney, G. A. Siviloglou, and D. N. Christodoulides, Science **324**, 229 (2009).
29. J. Arlt, V. Garces-Chavez, W. Sibbett, and K. Dholakia, Opt. Commun. **197**, 239 (2001).
30. J. Lin, J. P. B. Mueller, Q. Wang, G. Yuan, N. Antoniou, X.-C. Yuan, and F. Capasso, Science **340**, 331 (2013).